

8-22-2014

Assessing the fidelity of AOGCM-simulated relationships between large-scale modes of climate variability and wind speeds

Justin T. Schoof

Southern Illinois University Carbondale, jschoof@siu.edu

SC Pryor

Follow this and additional works at: http://opensiuc.lib.siu.edu/gers_pubs

Recommended Citation

Schoof, Justin T. and Pryor, SC. "Assessing the fidelity of AOGCM-simulated relationships between large-scale modes of climate variability and wind speeds." *Journal of Geophysical Research* 119, No. 16 (Aug 2014): 9719-9734. doi:10.1002/2014JD021601.

This Article is brought to you for free and open access by the Department of Geography and Environmental Resources at OpenSIUC. It has been accepted for inclusion in Publications by an authorized administrator of OpenSIUC. For more information, please contact opensiuc@lib.siu.edu.

RESEARCH ARTICLE

10.1002/2014JD021601

Key Points:

- US winds are strongly related to large-scale climate variability
- AOGCMs reproduce the basic characteristics of observed climate modes
- AOGCMs reproduce the basic links between climate modes and US winds

Correspondence to:

J. T. Schoof,
jschoof@siu.edu

Citation:

Schoof, J. T., and S. C. Pryor (2014), Assessing the fidelity of AOGCM-simulated relationships between large-scale modes of climate variability and wind speeds, *J. Geophys. Res. Atmos.*, 119, doi:10.1002/2014JD021601.

Received 1 FEB 2014

Accepted 31 JUL 2014

Accepted article online 5 AUG 2014

Assessing the fidelity of AOGCM-simulated relationships between large-scale modes of climate variability and wind speeds

J. T. Schoof¹ and S. C. Pryor²

¹Department of Geography and Environmental Resources, Southern Illinois University, Carbondale, Illinois, USA,

²Department of Earth and Atmospheric Sciences, Cornell University, Ithaca, New York, USA

Abstract The ability of atmosphere-ocean general circulation models (AOGCMs) to reproduce associations between surface/near-surface variables over the United States (US) and large-scale modes of climate variability has implications for evaluating possible biases in future climate projections and is an important model diagnostic. Indices of three such modes (El Niño–Southern Oscillation (ENSO), the Arctic Oscillation (AO), and the Pacific–North American (PNA) pattern) and their relationships to wind speeds over the contiguous US are derived using historical reanalysis products and then used to evaluate the fidelity of AOGCM simulations of both the climate modes and the teleconnections. In the reanalysis data, the response of middle and upper troposphere wind speeds to ENSO phase is found to be essentially symmetric with anomalies of opposite sign occurring during the warm and cold phases. The AO and PNA phases are both associated with higher wind speeds relative to “neutral” conditions. AOGCMs from Phase 5 of the Coupled Model Intercomparison Project (CMIP5) produce AO- and PNA-like spatial patterns which exhibit good accord with those from NCEP–NCAR Reanalysis. The AOGCM-derived climate indices also exhibit general agreement with reanalysis-derived indices in terms of the frequencies associated with highest variance, although the agreement is better for AO and PNA than it is for ENSO. The AOGCMs are in good agreement with the NNR in terms of representation of the influence of the AO and PNA on winds over the contiguous US. However, for ENSO, AOGCMs fail to consistently capture the observed relationship between La Niña and near-surface to middle troposphere winds.

1. Introduction

Near-surface and middle troposphere wind speeds exhibit variability across multiple time scales from seconds to decades. Large-scale modes of climate variability are at least partially responsible for variability on intramonthly to multidecadal timescales over the United States (US) [Enloe *et al.*, 2004; Klink, 2007; Pryor and Ledolter, 2010]. Tropospheric flow fields are used as a diagnostic of storm tracks [Grise *et al.*, 2013], play a role in mass and moisture advection [Lee *et al.*, 2014], and are coupled to near-surface wind speeds. Changes in near-surface wind speeds as a result of climate nonstationarity have great importance to range of socioeconomic sectors [see Pryor and Barthelmie, 2014]. Both dynamical and statistical downscaling of wind speeds have indicated high internal climate variability (linked in part to teleconnection indices) [Pryor *et al.*, 2012a] and have emphasized the importance of correctly capturing storm tracks and midtropospheric wind fields in developing robust wind climate projections [Pryor *et al.*, 2012b; Pryor and Barthelmie, 2014].

Previous studies of wind speeds in the context of large-scale climate variations have generally focused on a single teleconnection mode (e.g., El Niño–Southern Oscillation (ENSO)), a single atmospheric level, or a specific region, and on timescales of 1 month or longer. For example, Enloe *et al.* [2004] found that monthly mean peak wind gusts over the western US and Ohio River Valley increased (decreased) during La Niña (El Niño), particularly during the fall and winter months. Studies have also shown that 80 m wind speeds in the Great Lakes region [Li *et al.*, 2010] and 10 m wind speeds in the southern Canadian Prairies [St. George and Wolfe, 2009] vary with ENSO phase. Klink [2007] also found that monthly mean 70 m wind speeds in Minnesota were lower during El Niño and higher during the positive phase of the Arctic Oscillation (AO). Similarly, Pryor and Ledolter [2010] examined the relationship between the annual 90th percentile of radiosonde wind speeds (at 700 hPa in the western US and 850 hPa in the eastern US) and three prominent modes of Northern Hemisphere circulation variability (North Atlantic Oscillation (NAO), Pacific–North American pattern (PNA), and ENSO) and found that regionally averaged wind speeds exhibited significant

Table 1. Description of the CMIP5 AOGCMs Used in This Study^a

ID	Model	Institution	Resolution (Longitude × Latitude)	References
BCC	BCC-CSM1.1	Beijing Climate Center—China Meteorological Administration	2.8125° × 2.8125°	Wu [2012]; Xin et al. [2012]
BNU	BNU-ESM	Beijing Normal University, China	2.8125° × 2.8125°	Ji et al. [2014]
CAN	Can-ESM2	Canadian Centre for Climate Modelling and Analysis, Canada	2.8125° × 2.8125°	Arora et al. [2011]; von Salzen et al. [2013]
CNRM	CNRM-CM5	National Center for Meteorological Research, France	1.4° × 1.4°	Voltaire et al. [2012]
GFDL	GFDL-CM3	NOAA Geophysical Fluid Dynamics Laboratory, USA	2.5° × 2.0°	Delworth et al. [2006]; Donner et al. [2011]
HAD	HadGEM2-CC	Met Office, Hadley Centre, UK	1.875° × 1.25°	Bellouin et al. [2007]; Collins et al. [2008]; Martin et al. [2011]
IPSL	IPSL-CM5A-LR	Institut Pierre Simon Laplace, France	3.75° × 1.9°	Dufresne et al. [2012]
MPI	MPI-ESM-LR	Max Planck Institute for Meteorology, Germany	1.875° × 1.6°	Stevens et al. [2013]
MRI	MRI-CGCM3	Meteorological Research Institute, Japan	1.125° × 1.125°	Yukimoto et al. [2012]
NOR	NorESM1-M	Norwegian Climate Center, Norway	2.5° × 1.9°	Iversen et al. [2013]

^aModels are referenced by the ID throughout the paper.

differences with the phase of at least one mode in all regions of the contiguous US. Identification of strong statistical relationships between near-surface and lower troposphere wind speeds and large-scale modes of climate variability suggests that low frequency variability associated with these climate modes could be used to estimate low frequency wind variability using large-scale circulation features represented by AOGCMs [e.g., Klink, 2007].

Better understanding of the relationship between regional wind speeds and leading modes of climate variability thus has the potential to provide both an important diagnostic of climate models and to improve seasonal and long-term regional climate projections. To this end, our objectives are (1) to assess the relationship between large-scale modes of climate variability including ENSO, AO, and the PNA, and US wind speeds in reanalysis data, (2) to assess the fidelity with which contemporary AOGCMs simulate the main characteristics of these modes of variability, and (3) to examine the relationship between these modes of variability and US wind speeds in historical AOGCM simulations. Analyses presented herein employ data at a daily time step because the leading modes of Northern Hemisphere circulation variability, such as the AO and PNA, vary across a range of timescales, including intramonthly [Feldstein, 2002; Bamzai, 2003].

2. Data and Methods

2.1. Data Sources

The NCEP/NCAR reanalysis data set [Kalnay et al., 1996, hereafter referred to as NNR] is used as the reference dataset to characterize the climate modes and links to near-surface wind climates and flow fields over the contiguous US. We use daily NNR sea-surface temperatures (SST) on an approximately 1.9° × 1.9° Gaussian grid, and sea-level pressure (SLP) and wind speeds on a 2.5° × 2.5° grid for 1950–2005, corresponding to the standard historical period used in the experimental design of Phase 5 of the Coupled Model Intercomparison Project (CMIP5) [Taylor et al., 2012].

The AOGCMs used in this study are identified in Table 1 and are restricted to those with daily output for the historical period for all of the required variables. Additional details about the CMIP5 models can be found in Taylor et al. [2012]. The historical simulations used here are forced with historical greenhouse gas concentrations and time-evolving land cover. To facilitate direct comparison with NNR and between AOGCMs, output from all of the models was interpolated to the NNR 2.5° × 2.5° grid using a triangle-based linear interpolation. Interpolation may introduce errors and reduce AOGCM maxima. In this application, any errors are likely to be small given the focus on summary statistics derived from the daily mean wind field. In the remainder of the paper, the AOGCMs are referenced by the first three or four letters of the model name, representing the organization that developed the model (see Table 1).

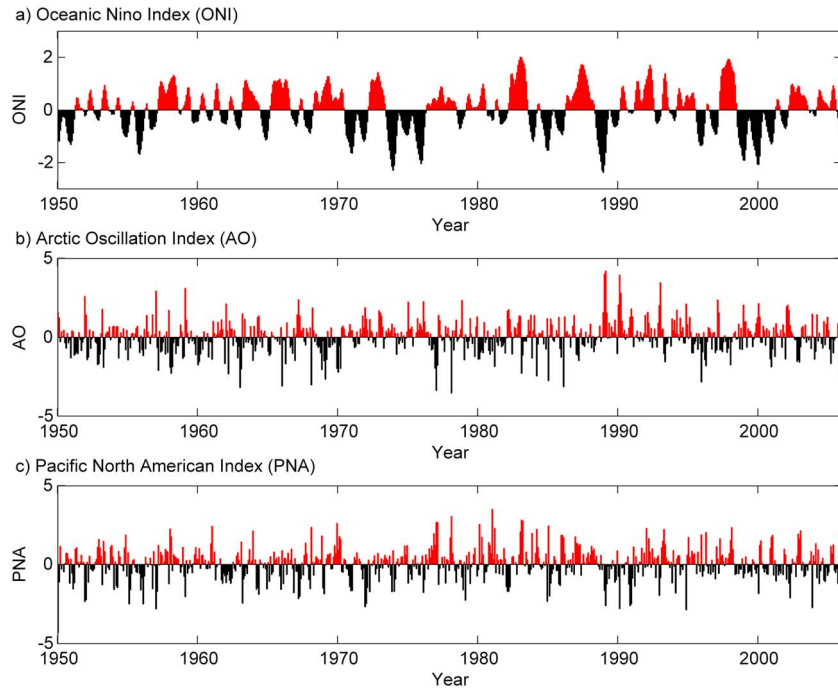


Figure 1. Time series of the monthly mean (a) Oceanic Niño Index (ONI), (b) Arctic Oscillation index (AO), and (c) Pacific North American pattern index (PNA) derived using output from NNR.

2.2. Calculation of the Climate Modes

We use a 3 month moving average of SST anomalies in the Niño 3.4 region (5°N–5°S, 170°–120°W) [Trenberth, 1997] to define the Oceanic Niño Index (ONI). Because warming has occurred in the tropical Pacific [Ashok et al., 2012], and additional future warming is likely, following the NOAA Climate Prediction Center, the base period used to define the anomalies changes every 5 years and is centered on the period of interest. Using this definition, we derive both daily and monthly (Figure 1a) ONI time series. The monthly ONI presented here has been demonstrated by Trenberth [1997] to capture the major characteristics of SST variability in the tropical Pacific Ocean. It is highly correlated ($r = 0.8$) with the multivariate ENSO index (MEI) [Wolter and Timlin, 1993]. The ONI is also used operationally by NOAA to assess historical ENSO variability and place current conditions in a historical context. The recent study of Kim and Yu [2012] evaluated the SST patterns associated with central Pacific (CP) and eastern Pacific (EP) types of ENSO events. Here, we focus on the teleconnection between ENSO variations and Northern Hemisphere circulation variability by regressing the ONI time series onto the hemispheric 500 mb geopotential height field. The pattern, shown in Figure 2a, indicates that warm events

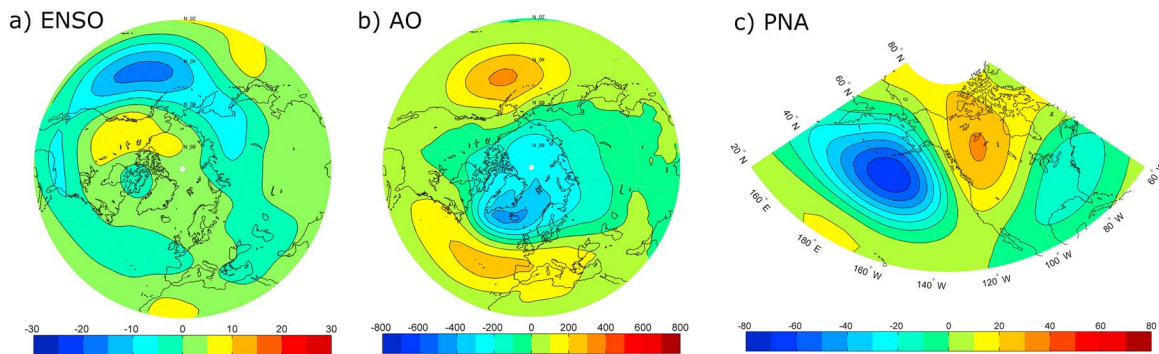


Figure 2. Spatial patterns of Northern Hemisphere circulation associated with (a) El Niño–Southern Oscillation (ENSO; m), (b) the Arctic Oscillation (AO; Pa), and (c) the Pacific North American mode (PNA; m) as derived using output from NNR. The patterns represent the 500 hPa geopotential height (ENSO, PNA) or SLP (AO) field regressed on the associated index.

Table 2. Percentage of Days (1950–2005) by Season Corresponding to the Positive, Neutral, and Negative Phase of the Arctic Oscillation (AO), Pacific North American Mode (PNA), and El Niño–Southern Oscillation (ENSO) Based on Analysis of NNR

	AO			PNA			ENSO		
	POS	NEUT	NEG	POS	NEUT	NEG	POS	NEUT	NEG
DJF	5.9	12.8	6.0	5.9	13.0	5.7	2.1	17.2	5.1
MAM	3.9	17.4	3.9	3.9	17.6	3.7	4.3	20.7	<0.1
JJA	1.0	23.0	1.2	1.8	22.6	1.2	3.0	21.3	1.0
SON	2.9	19.0	3.0	3.1	18.3	3.4	2.1	17.7	5.1

(El Niños) are characterized by lower heights across the central Pacific Ocean and southern US and higher heights across northwestern North America. The opposite response is expected under cold events (La Niñas).

The North Atlantic versus truly annular nature of Northern Hemisphere climate variability is a subject of debate [cf. *Ambaum et al.*, 2001 and *Wallace and Thompson*, 2002]. Here, we adopt the AO paradigm, but also consider separately variability in the Pacific sector using the PNA index, and note the high correlation between metrics of the North Atlantic Oscillation (NAO) and AO at the monthly time step [*Deser*, 2000]. We define the AO as the leading empirical orthogonal function (EOF) of sea-level pressure north of 20°N, using area-weighted data and a base period of 1950–2005. The resulting pattern is a dipole with opposite sign in the northern polar region and a band centered at approximately 45°N (Figure 2b). The two prominent regions of variability in the outer ring, located in the Euro-Atlantic sector and in the central Pacific Ocean, have uncorrelated sea-level pressure anomalies, largely because the second EOF is associated with centers of action of opposite sign in those same two regions [*Wallace and Thompson*, 2002]. The time series of the first EOF (Figure 1b) is referred to as the AO index and regression onto the hemispheric SLP field produces the characteristic AO pattern (Figure 2b). This EOF explains 14.3% of the variance in the NH SLP field in the NNR data. The monthly AO index derived this way correlates highly ($r = 0.93$) with the NOAA Climate Prediction Center definition based on 1000 hPa heights.

The PNA index is defined as the leading EOF of the 500 hPa geopotential height field in the Pacific-North American sector (150°E to 60°W, 20°N to 80°N) following *Stoner et al.* [2009]. Regression of the PNA index onto the 500 hPa geopotential height field produces the characteristic PNA wave train pattern with areas of low height over the north Pacific region and the southeast US and a ridge over the western US (Figure 2c). This index correlates highly ($r = 0.86$) with the original four-grid point PNA definition of *Wallace and Gutzler* [1981].

To quantify the relationship between indices of ENSO, AO, and PNA and US wind speeds, each day is classified as exhibiting positive, neutral, or negative phase conditions for each index. The mean and 90th percentile wind speeds at 10 m above the surface (hereafter 10 m) and on three lower to midtropospheric pressure levels (850 hPa, 700 hPa, and 500 hPa) in the NNR data and AOGCM output are computed for each grid cell and index class. For ENSO, values of ONI > 0.5 were considered positive (warm phase, or El Niño), while ONI < -0.5 were considered negative (cold phase, or La Niña). The AO and PNA indices are both standardized, so values > 1.0 (1 standard deviation above the mean) were considered positive, while values < -1.0 were considered negative. For all three indices, all other values were classified as neutral. Each index exhibits the greatest (least) variability during the cold (warm) season, but days characterized by each phase occur in all climatological seasons (Table 2). Thus, the teleconnections between the climate modes and winds over the contiguous US presented are derived for the whole calendar year.

In section 3, we quantify the association between each climate mode and wind speeds by examining differences in mean and 90th percentile values under the positive and negative phase of each index relative to neutral conditions using the NNR. To test the significance of differences in mean wind speed, we conduct two-tailed t tests assuming unequal variance and using an effective sample size (n) to account for temporal autocorrelation in the series. For the 90th percentiles, we employ a nonparametric sign test [see, e.g., *Burt et al.*, 2009]. Under the null hypothesis that the 90th percentile wind speeds are the same under two phases, 10% of the wind speeds from one phase should be greater than the 90th percentile wind speed from the other phase. The test then simplifies to a test for a population proportion equal to 10% ($H_0: \pi = 0.1$). Under the null hypothesis, the sampling distribution of proportions has a standard normal distribution with mean $P_{90} - 0.1$ and standard deviation $\sqrt{(0.1)(0.9)/n}$.

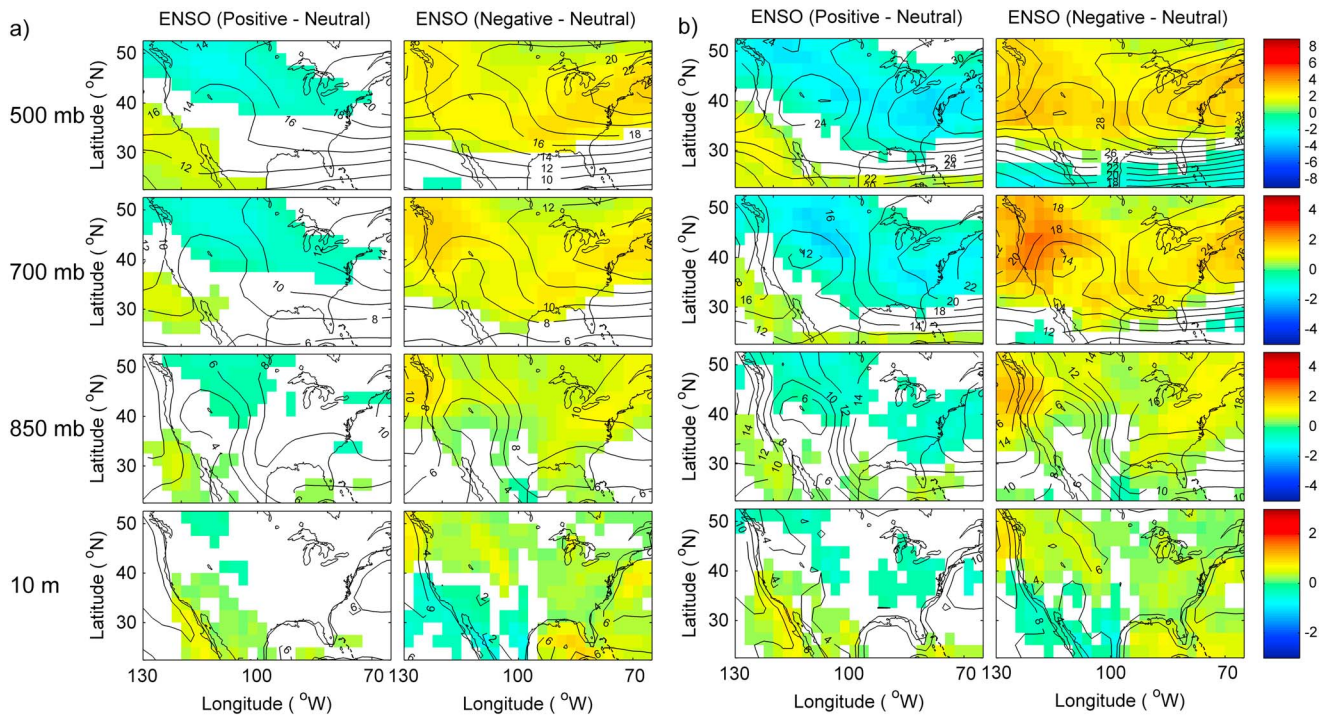


Figure 3. Differences in (a) mean and (b) 90th percentile wind speeds (m s^{-1}) during the positive (left column) and negative (right column) phases of El Niño–Southern Oscillation (ENSO) relative to neutral conditions. The colors denote the magnitude of the wind speed differences (m s^{-1}) and are shown only where the differences are statistically significant at the 99% confidence level. The contours show the actual wind speeds (m s^{-1}) at each level for each ENSO phase. The results are based on output from NNR.

3. Teleconnections Between ENSO, AO, PNA, and US Wind Speeds in NNR

3.1. El Niño–Southern Oscillation (ENSO)

ENSO affects US wind speeds primarily through changes in midlatitude cyclone tracks associated with changes in the position of subtropical and polar jet streams [e.g., Eichler and Higgins, 2006]. Accordingly, the positive ENSO phase is characterized by a stronger subtropical jet and therefore slightly higher midtropospheric mean and 90th percentile wind speeds over the southern US. The 500 hPa height expression of ENSO (Figure 2a) suggests that both the subtropical high pressure over the Pacific sector and the subpolar low are enhanced during La Niña, leading to stronger westerlies across North America. Consistent with analyses of radiosonde data [Pryor and Ledolter, 2010] and near-surface wind speeds [e.g., Li et al., 2010], the positive ENSO phase is associated with considerably lower midtropospheric mean and 90th percentile wind speeds over the northern US (Figure 3). Conversely, the negative ENSO phase is associated with a more northerly storm track [Grise et al., 2013] and higher wind speeds particularly at the 500 hPa level. For example, compare the upper two panels in Figure 3b which show 500 hPa wind speed anomalies in the positive and negative ENSO phase relative to the neutral phase. These differences in wind speeds by ENSO phase are less pronounced closer to the surface (Figure 3). Wind speeds at 10 m exhibit few regions (largely confined to the southwest US) of significant difference under the positive ENSO phase. However, the negative ENSO phase (La Niña conditions) is associated with significantly stronger 10 m wind speeds over most of the US and significantly weaker 10 m wind speeds in the extreme southwest US (Figure 3).

3.2. Arctic Oscillation (AO)

The positive phase of the AO is associated with increased midtropospheric wind speeds relative to conditions during neutral AO periods over the entire US, with the largest differences for the southern and eastern states (Figure 4). Nearer to the surface, topography modifies this pattern, but consistent with prior research (e.g., Klink [2007] over Minnesota), positive AO conditions are associated with significantly higher 850 hPa and 10 m wind speeds over the most of the contiguous US. The negative phase of the AO is associated with a

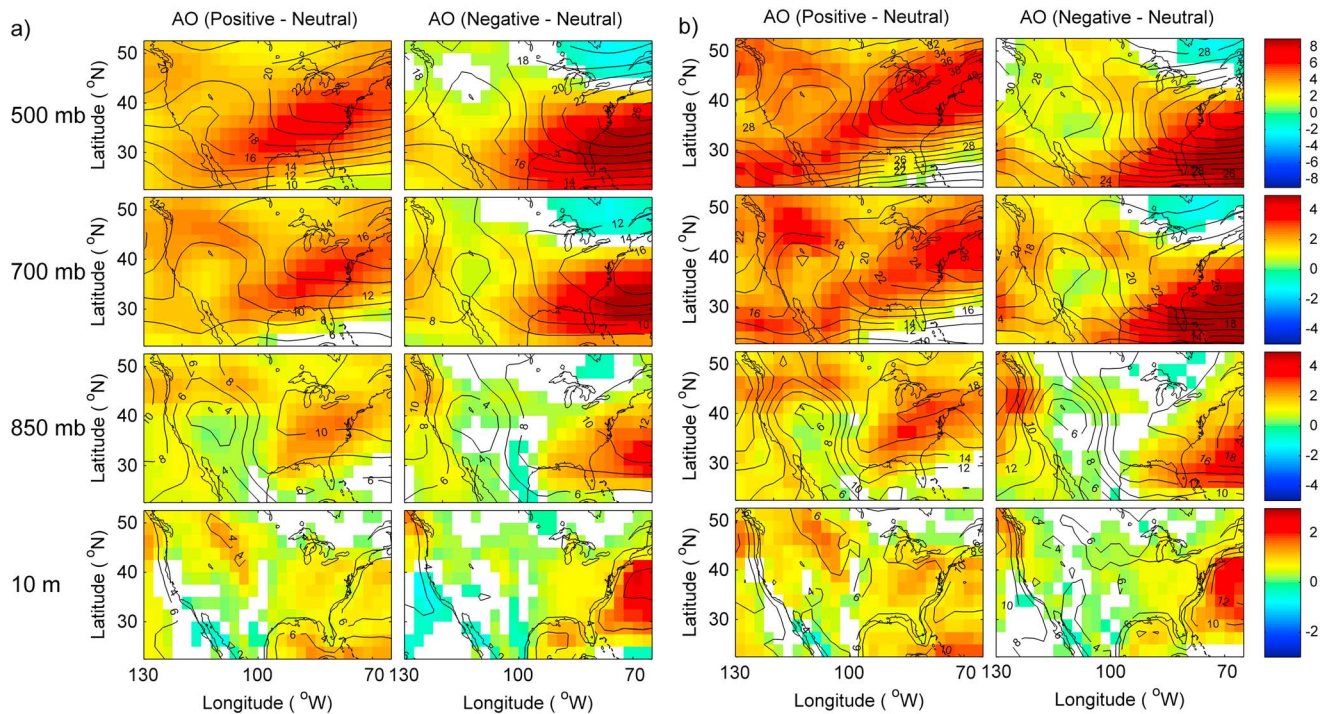


Figure 4. As in Figure 3, but for the Arctic Oscillation (AO).

more zonal pattern over the eastern US but more northerly flow over the north-central US which is often associated with cold weather extremes during winter [Griffiths and Bradley, 2007; Cohen et al., 2010; L'Heureux et al., 2010]. Despite the difference in large-scale circulation between the positive and negative AO phases, midtropospheric wind speeds also tend to be higher during negative AO conditions relative to neutral (Figure 4). The location of the maximum enhancement of wind speed is displaced in the positive AO phase toward the southeast extending over the western subtropical Atlantic Ocean (Figure 4). Differences in 90th percentile wind speeds under the positive and negative AO phases exhibit the same general patterns as the mean wind speeds but are generally of slightly larger magnitude (cf. Figures 4a and 4b). Increases in wind speeds under the positive phase of the AO appear to be related to the enhanced latitudinal pressure gradient and therefore occur throughout the study region. During the negative phase, the increase is related to changes in jet stream position that primarily impact the eastern US by changing the jet stream configuration to a more meridional pattern (i.e., a low zonal index).

3.3. Pacific-North American Pattern (PNA)

The positive PNA phase is associated with strong midtropospheric ridging in the western US with lower heights in the eastern US, while the negative phase is associated with enhanced zonality (cf. Leathers et al. [1991] and Figure 5). Relative to the neutral phase, as in Pryor and Ledolter [2010], the negative PNA phase is associated with significantly higher midtropospheric wind speeds over much of the contiguous US (Figure 5). Higher wind speeds in the positive PNA phase are confined to the eastern USA and a small number of grid points exhibit significantly lower 10 m wind speeds under positive PNA conditions, likely due to a strengthening of the Great Basin high under positive PNA conditions [Sheridan, 2003]. For both the mean and 90th percentile winds, the region of lower wind speeds associated with the positive PNA phase extends from the 500 hPa level to 10 m. Averaged across significant grid points, differences in the 90th percentile wind speeds in the eastern US tend to be of higher magnitude than those described for the mean wind speeds, indicating that, as with ENSO and AO, the impact of the PNA on atmospheric flow over the contiguous US is amplified in the upper tail of the wind speed probability distribution.

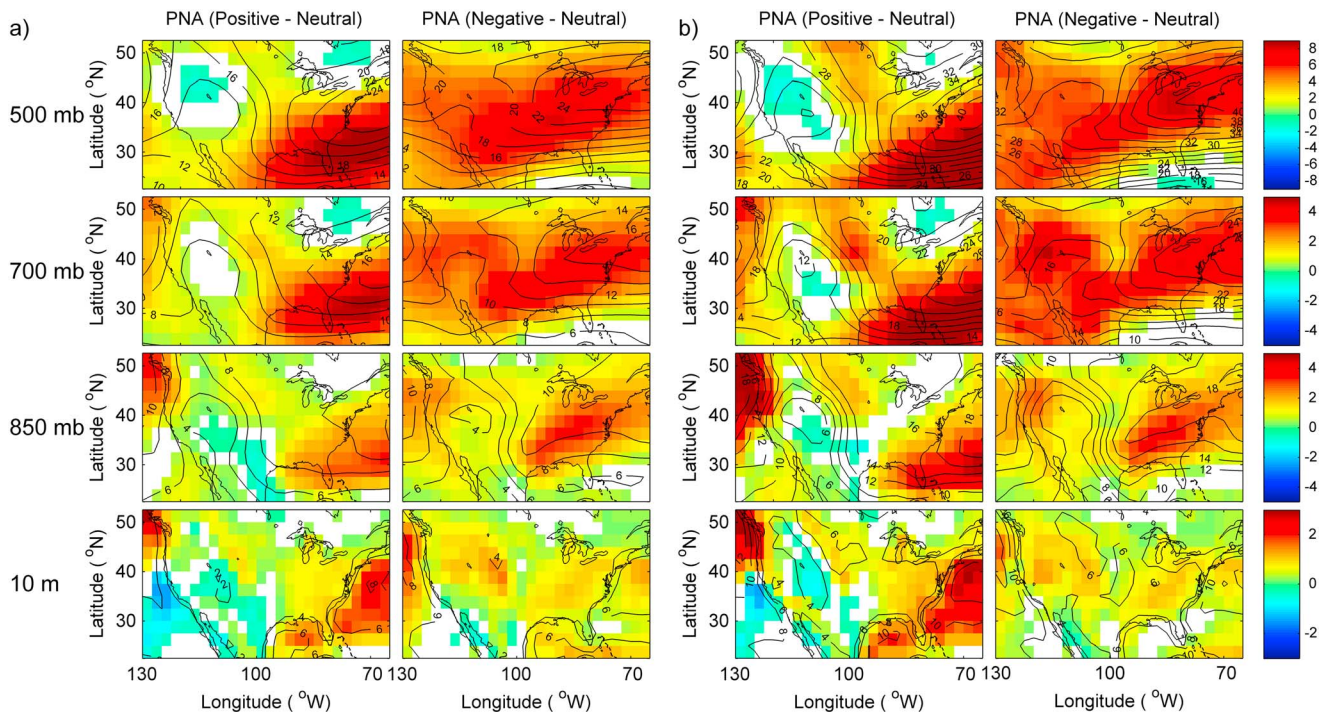


Figure 5. As in Figure 3, but for the Pacific-North American (PNA) pattern.

4. Simulation of ENSO, AO, and PNA by CMIP5 AOGCMs

To evaluate the fidelity of the CMIP5 AOGCMs in terms of the representation of ENSO, AO, and PNA, we compared both the spatial and temporal characteristics of the AOGCM-simulated modes (computed as described in section 2) relative to NNR. For each mode, we computed both a time series and a spatial pattern using methods identical to those applied to the reanalysis data. The reproduction of large-scale circulation patterns associated with modes of variability are assessed in part using *Taylor* [2001] diagrams, which allow visualization of the Pearson product-moment correlation coefficient (r), the spatial standard deviation, and the root mean square error (RMSE) on a single two-dimensional plot. The temporal characteristics are assessed primarily using spectral techniques to identify variability across timescales.

The AOGCMs considered here generally reproduce a spatial pattern that qualitatively resembles the observed 500 hPa response to ENSO (Figure 6) but with substantive differences among the models. The NNR derived pattern is characterized by a region of low heights across the central Pacific and extending both across the US and into northeast Asia. A region of higher heights is present over northwestern North America. All of the AOGCMs exhibit similar features, although the pattern intensity and position differs greatly. The majority (7 of 10 AOGCMs) overestimates the intensity of the high latitude center of action relative to the NNR reference, and several models extend the region of higher heights to include the North Atlantic region. Pattern correlations between the NNR and CMIP5 models range from less than 0.5 (MRI) to above 0.8 (BNU and HAD; Figure 7a). Seven of the 10 AOGCMs exhibit patterns with too much spatial variability (higher spatial standard deviation). The models with the lowest pattern RMSE relative to NNR are BCC, BNU, and CNRM (Figure 7a).

All of the AOGCMs also produce a pattern that is similar to the NNR AO pattern (Figure 8). However, consistent with prior analyses of CMIP2 [Stephenson *et al.*, 2006] and CMIP3 [Stoner *et al.*, 2009] generation AOGCMs, the variance explained by the first EOF from the CMIP5 AOGCMs (15.1–23.2%) is larger than in NNR (14.3%). Approximately half of the models presented here overestimate the magnitude, and often the spatial extent, of the polar center of action of the AO, which is in contrast to the CMIP3 AOGCMs examined by Stoner *et al.* [2009]. Most models presented in Figure 8 reproduce the magnitude (with a slight positive bias) and position of the North Pacific center of action of the AO, although MRI-CGCM3 exhibits a clear negative bias in this feature. The AOGCMs have a general tendency to shift the North Atlantic center of action toward Western

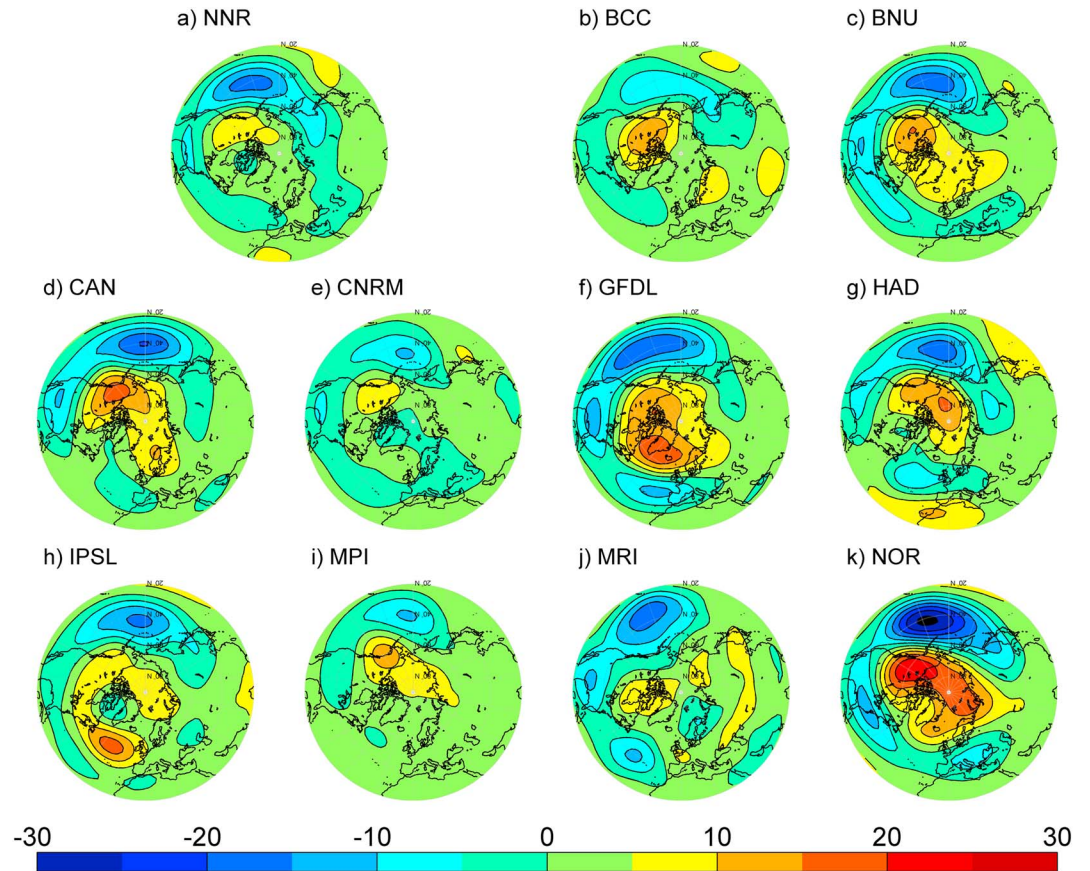


Figure 6. The spatial pattern of the Northern Hemisphere circulation response to ENSO in the NNR and 10 CMIP5 AOGCMs. The patterns show 500 hPa geopotential height anomalies (m) and are derived by regressing the 500 hPa geopotential height field against the NNR or AOGCM derived Oceanic Niño Index (ONI).

Europe, and two AOGCMs (HAD and IPSL) substantially underestimate the intensity of the North Atlantic center of action (Figure 8). Most of the models exhibit strong pattern correlations with NNR ($r > 0.85$), but several overestimate the spatial variability in the pattern relative to NNR (Figure 7b). Only HAD underestimates the spatial variability in the pattern and the spatial variability in CAN closely matches that in the NNR data. The AOGCMs with the pattern most closely resembling the NNR reference are CAN and GFDL (Figure 7b).

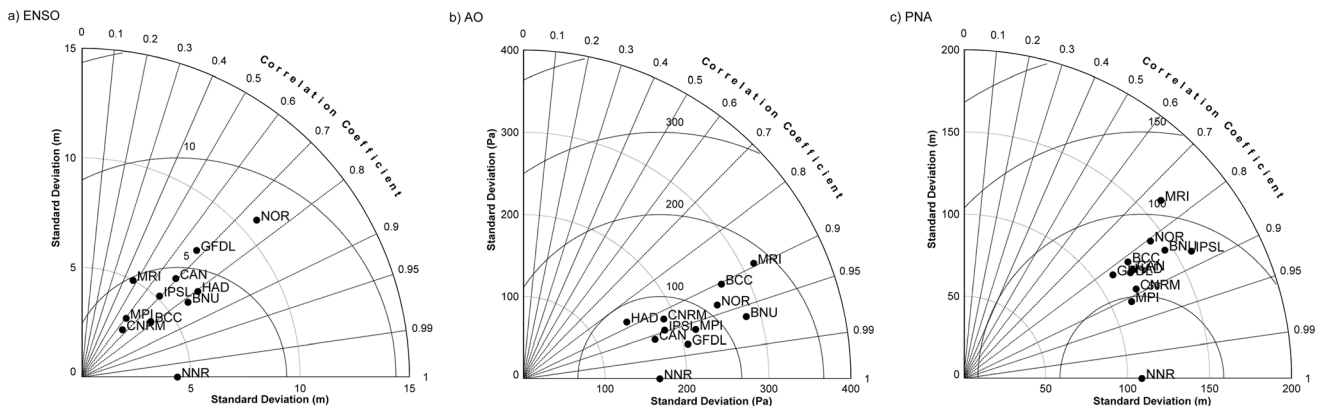


Figure 7. Taylor diagrams for (a) ENSO, (b) AO, and (c) PNA. The x axis and y axis are the spatial standard deviations, and the radial axis is the spatial correlation between the NNR and AOGCM patterns. The distance between each AOGCM point and the NNR represents the root mean square error (RMSE).

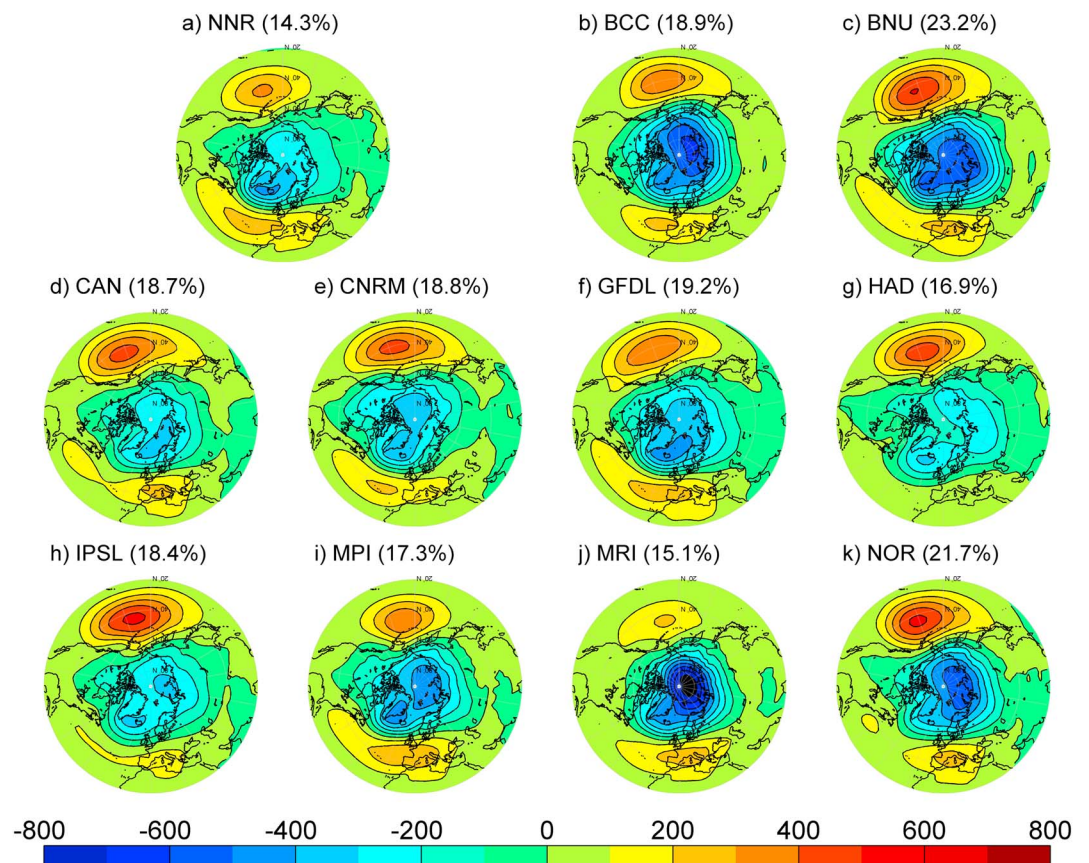


Figure 8. The spatial pattern of the Northern Hemisphere circulation response to the Arctic Oscillation (AO) in the NNR and 10 CMIP5 AOGCMs. The patterns show sea level pressure (SLP) anomalies and are derived by regressing the sea-level pressure field against the NNR or AOGCM derived AO index (the first EOF of the SLP field). The numbers shown in parentheses above each frame give the variance explained by this EOF.

All of the AOGCMs also exhibit PNA patterns that resemble the NNR pattern (Figure 9). The variance explained by the PNA pattern in the AOGCMs ranges from 21.0% to 30.5%, which is in relatively good accord with NNR (24.5%), and is consistent with the relatively good fidelity of the PNA over North America as manifest in CMIP3 generation AOGCMs [Stoner *et al.*, 2009]. However, there is substantial variability among the models in terms of the magnitude of the individual centers of action. The North Pacific center of action is too pronounced in several models (BCC, BNU, NOR) and too weak in others (e.g., CAN and GFDL). Similarly, the BNU, CAN, GFDL, MPI, and NOR models overestimate the magnitude of the Atlantic center of action (Figure 9). The Taylor diagram for the PNA indicates slightly lower pattern correlations than are evident for AO, ranging from approximately 0.75 (MRI) to above 0.9 (MPI) (Figure 7c). All AOGCMs overestimate the magnitude of the PNA pattern, with GFDL and MPI producing spatial variability that most closely approximates that in the NNR pattern. The pattern RMSE relative to NNR is lowest in the MPI model (Figure 7c).

To examine the key modes of temporal variability, power spectra were computed from the daily time series of the three modes as computed from NNR, European Centre for Medium-Range Weather Forecasting (ECMWF) ERA-Interim reanalyses [Dee *et al.*, 2011], and the AOGCMs. Indices computed from the NNR and shorter (1979–2005) ECMWF reanalysis data set exhibit very similar dominant modes of temporal variability for each of the indices (Figure 10), which lends credibility to use of NNR as the reference for the AOGCMs comparison.

Consistent with prior research that has indicated that the CMIP5 AOGCMs still do not capture the seasonal timing of ENSO [e.g., Sheffield *et al.*, 2013b], the index that exhibits least agreement between the reanalyses and the AOGCMs is ENSO (Figure 10a). While the ENSO index from NNR exhibits a peak in variance at a time scale that equates to a period of approximately four years (i.e., $f \sim 8 \times 10^{-4} \text{ d}^{-1}$), several of the AOGCMs (notably BNU) exhibit higher variance associated with frequencies of $2\text{--}3 \times 10^{-3} \text{ d}^{-1}$ (i.e., periods of ~ 1 year)

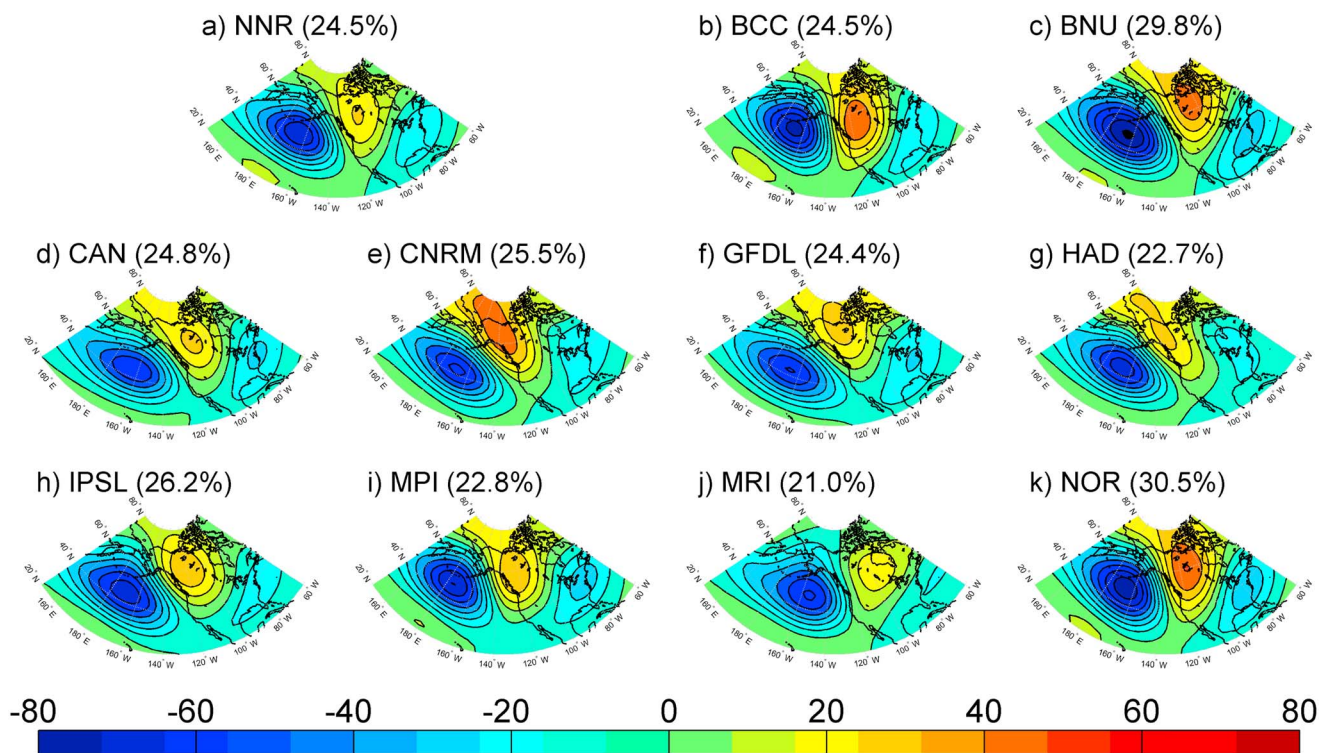


Figure 9. The spatial pattern of the circulation response to the PNA pattern in the NNR and 10 CMIP5 AOGCMs. The patterns show the 500 hPa geopotential height anomalies (m) and are derived by regressing the 500 hPa geopotential height field against the NNR or AOGCM derived PNA index (the first EOF of the 500 hPa field). The numbers shown in parentheses above each frame give the variance explained by this EOF.

than is manifest in NNR. A different group of models (e.g., BCC and GFDL) also appear to indicate considerably higher variance at $f \sim 1.2 \times 10^{-3} \text{ d}^{-1}$ (period ~ 2.3 years).

Peak variance in the AO time series are focused at periods of approximately 100 days and are relatively consistent between the reanalysis and AOGCM output (Figure 10b), although three models (BNU, GFDL, and NOR) also exhibit variance at multi-year periods that do not appear to be present in NNR, ECMWF, or the other AOGCMs considered. The AOGCM that exhibits highest RMSE for the AO pattern relative to NNR (i.e., MRI; see Figure 7b) does not exhibit anomalous temporal variability (Figure 10b) which emphasizes the value in considering both the time and space domains in the assessment of model fidelity.

The AOGCMs exhibit greatest accord with the NNR for the PNA with the majority exhibiting maximum variance at frequencies $\sim 2 \times 10^{-2}$ to $6 \times 10^{-2} \text{ d}^{-1}$ (i.e., periods ~ 16 – 50 days; Figure 10c). The only exception is CNRM which indicates highest variance associated with frequencies $< 2 \times 10^{-2} \text{ d}^{-1}$ (Figure 10c). The MRI AOGCM exhibits the poorest representation of PNA relative to NNR in terms of the spatial pattern (Figure 7c). However, relatively good accord was found in terms of temporal variability (Figure 10c). Conversely, MPI, which exhibits “best” agreement in terms of the metrics included in the Taylor diagram (Figure 7c), is shifted toward variability at lower frequencies relative to NNR.

These analyses indicate that as in previous evaluations of the CMIP5 AOGCM suite (e.g., in terms of hydrological and thermal regimes over North America [e.g., Sheffield et al., 2013a, 2013b] and in terms of ENSO indices [e.g., Langenbrunner and Neelin, 2013]), no individual model uniformly out-performs the others. This provides an important justification for including all AOGCMs in the analysis of teleconnections, since no one model consistently exhibited anomalous performance (positive or negative) in terms of reproducing the climate modes.

Although this evaluation exercise indicates some failings in terms of the ability of the CMIP5 AOGCMs to represent the spatial and temporal characteristics of the leading modes of climate variability, the skill apparent in the ten AOGCMs presented herein is deemed sufficient to warrant analysis of the relationship between simulated large-scale modes of climate variability and regional wind speeds relative to

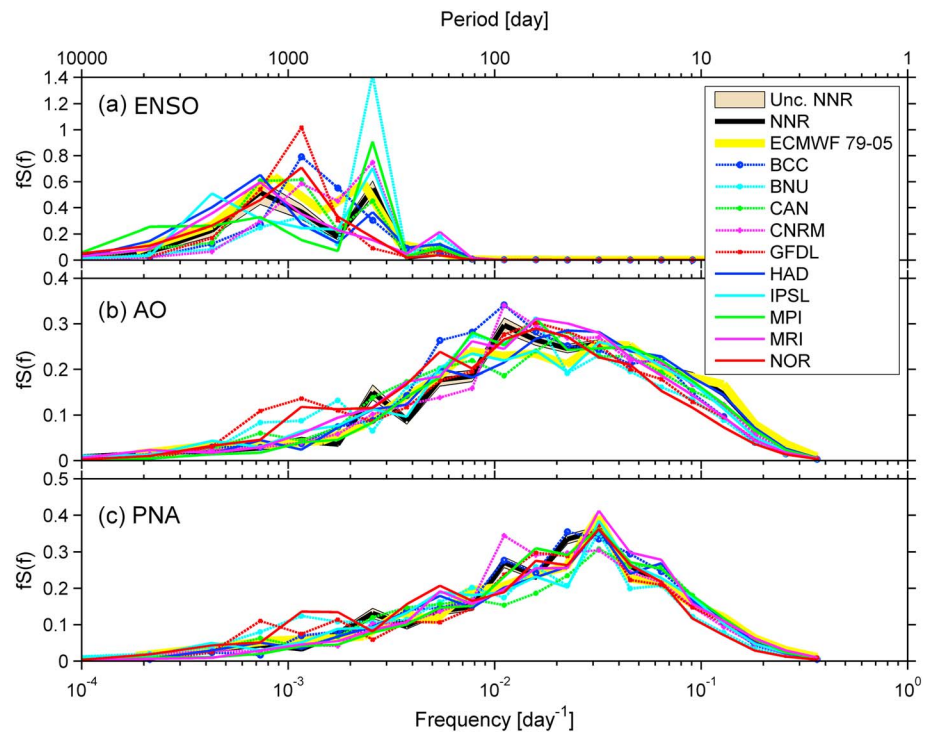


Figure 10. Power spectra for (a) ENSO, (b) AO, and (c) PNA based on daily time series of indices for 1950–2005 from NNR, ECMWF ERA-Interim reanalysis, and the AOGCMs. Also shown for the NNR power spectra is the uncertainty region computed assuming that each Fourier mode is normally distributed and uncorrelated with other modes. The spectra are shown as frequency \times spectral energy density ($f \times S(f)$) versus frequency (f) (or period on the top axis) on semilog graphs so that the area under any portion of the curve is proportional to the variance.

teleconnections manifest in the NNR. Since no single model stands out in terms of best or worse performance across all metrics, we consider each of the models and present results in terms of the multi-model ensemble (MME).

5. Teleconnections Between ENSO, AO, PNA, and Wind Speeds Over the Contiguous US in CMIP5 AOGCMs

To determine the extent to which teleconnections between the climate modes and near-surface to middle troposphere flow over the contiguous US as manifest in NNR are reproduced by contemporary (CMIP5) AOGCMs, the analyses described in section 3 were repeated with each of the AOGCMs described in section 2. Because there is similarity between relationships at 500 hPa and 700 hPa and also between relationships at 850 hPa and 10 m, results are presented only for the highest (500 hPa) and lowest (10 m) levels. To facilitate synthesis of the 10 AOGCMs considered, we present the results in terms of (1) the MME response to each phase of ENSO, AO, and PNA and (2) the number of models (out of 10) that agree with the reanalysis data regarding the sign of the response to each phase of ENSO, AO, and PNA.

5.1. El Niño–Southern Oscillation (ENSO)

Consistent with analyses presented in section 4 that indicated the CMIP5 AOGCM simulations of ENSO are improved relative to previous generations of models, but remain inconsistent among AOGCMs, the observed teleconnections between ENSO and wind speeds over the contiguous US are not fully reproduced in the climate models.

In NNR and observational data, the positive ENSO phase (El Niño) is generally associated with higher values of the mean and 90th percentile 500 hPa wind speeds over the southern US and lower 500 hPa mean and 90th percentile wind speeds over the northern US with the opposite response to the negative (La Niña) phase of ENSO (Figure 3a). The CMIP5 AOGCMs generally reproduce the pattern of the 500 hPa wind

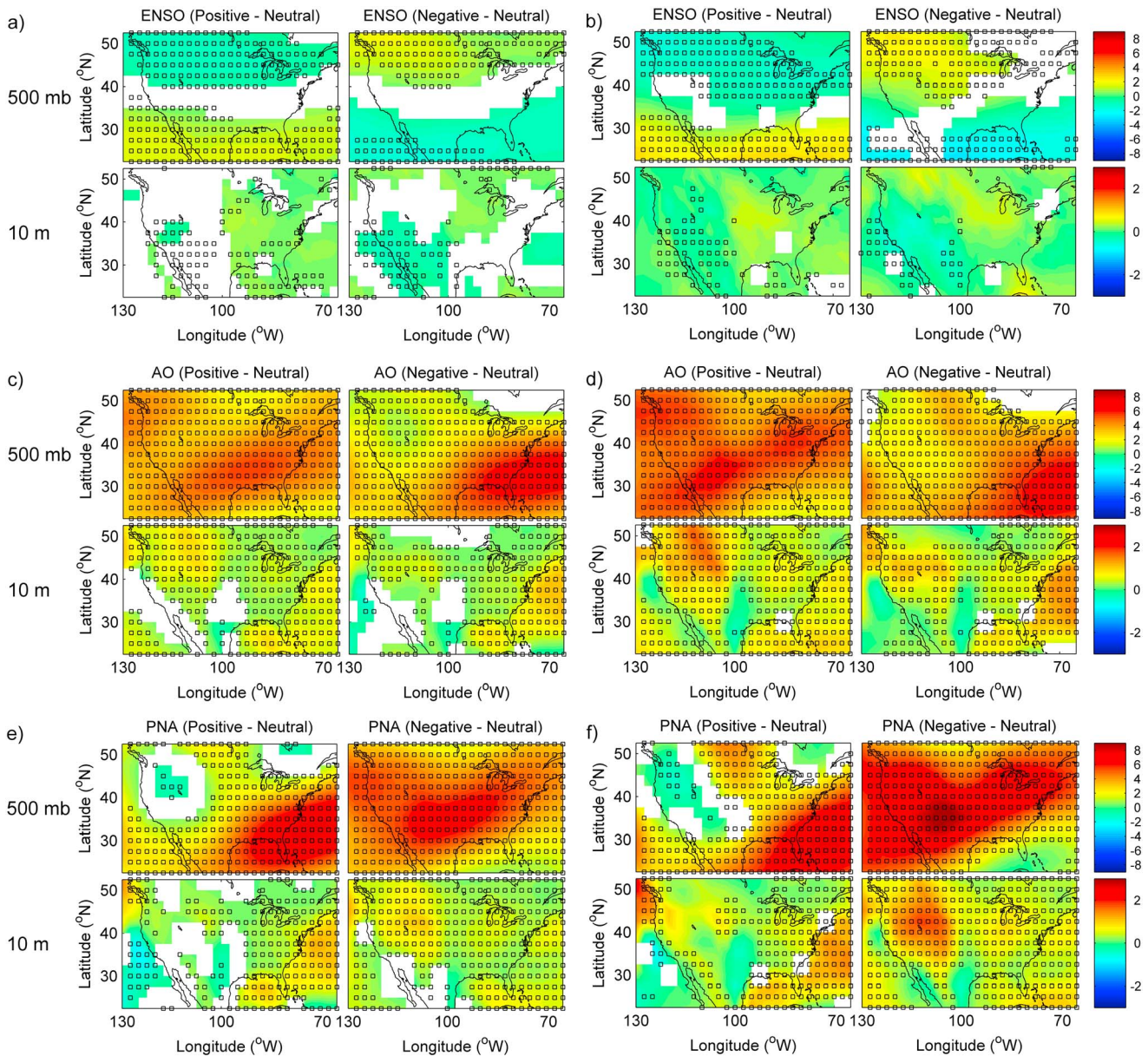


Figure 11. AOGCM simulated response in (left) mean and (right) 90th percentile wind speeds to the positive and negative phases of (a, b) ENSO (ONI), (c, d) AO, and (e, f) PNA. The colors indicate the ensemble mean response of the 10 AOGCMs considered in $m\ s^{-1}$ and are only shown where the differences are statistically significant at the 99% confidence level. The presence of a square indicates that at least 8 of the 10 AOGCMs agree with NNR on the sign of the difference.

response to El Niño, but with some differences in the magnitude of the response (cf. Figures 3a, 3b, 11a, and 11b). At least 8 of 10 AOGCMs agree with NNR in terms of the sign of the warm phase wind anomaly relative to the neutral phase in the same regions where significant relationships exist in the NNR data (Figures 3a, 3b, 11a, and 11b). During La Niña, the CMIP5 AOGCMs displace the region of positive wind speed anomalies north relative to NNR (cf. Figures 3b and 11b). Also, while in NNR the difference in wind speeds between the negative and neutral phase is statistically significant over almost the entire US (Figures 3a and 3b), the majority of the AOGCMs only reproduce a difference in wind speeds in the far northern and far southern parts of the study area (Figures 11a and 11b).

A significant response to ENSO phase is evident in 10 m wind speeds from NNR in the southwest and in the high elevations of the Rocky Mountains during El Niño and over most of the domain during La Niña (Figures 3a and 3b). The CMIP5 AOGCMs reproduce the sign of the NNR response to El Niño in the southwest,

with at least 8 of the 10 AOGCMs indicating the same sign of wind speed response to that in the NNR (Figure 11a). However, the differences between El Niño and neutral conditions in this region are not statistically significant. The response of the mean 10 m wind speed to La Niña is only reproduced over a small part of the southwest and in a narrow region of the Great Plains (Figure 11a). The 90th percentile of the 10 m winds shows better agreement with the NNR, but the magnitude of the response is underestimated in the Southeast US and differs in sign over parts of the West (cf. Figures 3b and 11b).

5.2. Arctic Oscillation (AO)

Consistent with the relatively good representation of the AO in the CMIP5 AOGCMs (section 4), the 500 hPa wind speed response to the phase of the AO as manifest in NNR is reproduced by most or all of the CMIP5 AOGCMs (cf. Figures 4, 11c and 11d). The models agree with NNR with respect to the sign of the wind speed response to both positive and negative AO conditions, although the magnitude of the mean AOGCM response is smaller than the observed response in some regions, such as the southeast US. The overwhelming majority of grid cells have ≥ 8 AOGCMs that agree with NNR in terms of the sign of response in wind speed and a range of responses (not shown) that is smaller than the observed difference in wind speed for a given AO phase (Figures 11c and 11d), reflecting a robust and consistent response to the AO across the models. For example, averaged over the Pacific Northwest (40°N–50°N, 125°W–115°W) the spread in response of the mean 500 hPa wind speed to the positive phase AO is $\leq 2.25 \text{ m s}^{-1}$, while the mean 500 hPa wind speed is approximately 16 m s^{-1} and the difference in wind speed in NNR from positive to neutral phase is $\sim 3 \text{ m s}^{-1}$.

Nearer to the surface, the AOGCMs also show a high level of agreement with teleconnections derived from NNR data in terms of sign. However, the AOGCM simulated differences in 10 m winds between phases is small relative to the NNR in some regions, such as the Southeast US. In general, the range of AOGCM responses is proportional to the magnitude of the difference in the reference dataset. As an example, 10 m wind speeds in the high elevations of the Rockies increase when the AO is positive (Figures 4a and 4b). All of the models also exhibit higher wind speeds in this region when the AO is positive (Figures 11c and 11d), but there is a large range among AOGCM responses (not shown). In the southwest and along the front range of the Rocky Mountains, the observed (NNR) relationship between 10 m wind speeds and the AO index is characterized by sharp spatial gradients with grid cells exhibiting significantly weaker wind speeds adjacent to grid cells with significantly stronger wind speeds (Figure 4). Winds in this region are influenced not only by the large topographic relief but also by the Great Plains Low-Level Jet (GPLLJ), which has been shown to be influenced by the position of the Bermuda-Azores high, one of the midlatitude centers of action for the AO [Weaver and Nigam, 2008; Coleman and Budikova, 2013]. In a study of CMIP3 models, Cook *et al.* [2008] found that models exhibited widely varying accuracy with respect to the GPLLJ. Sheffield *et al.* [2013a] identified shortcomings related to spatial extent and seasonal timing of the GPLLJ in CMIP5 models. The CMIP5 models considered here exhibit a response to AO that is of the right sign, but smaller in magnitude than the observed response, suggesting that the AO teleconnections to regional-scale lower to mid tropospheric winds is too weak in this region.

5.3. Pacific-North American Pattern (PNA)

The CMIP5 AOGCMs analyzed herein reproduce the spatiotemporal patterns of the PNA (section 4), and also agree with NNR analyses with respect to the 500 hPa wind speed response to PNA phase (cf. Figures 5, 11e and 11f). For both the positive and negative PNA phases, the AOGCMs nearly universally agree with each other and the NNR in terms of the sign of the effect of the PNA on 500 hPa wind speeds, with some regional variation in the magnitude of the wind response. In many regions, agreement in the sign of the differences between PNA phases is accompanied by a small range of AOGCM responses (not shown), especially in the case of the positive PNA phase. Nearer to the surface (at 10 m), the overall fidelity of the AOGCM-derived PNA response varies by region. In the eastern US, models consistently reproduce the increase in wind speeds associated with both PNA phases, albeit with smaller magnitude than the NNR (cf. Figures 5a and 11e). The models also exhibit agreement on the response to both PNA phases in the northwest with lower wind speeds at 500 hPa in the positive phase (cf. Figures 5, 11e, and 11f). In the southwest US, the response to negative PNA (significantly stronger winds) is consistently reproduced, but the response to positive PNA (significantly weaker winds at both 500 hPa and 10 m) is not consistently reproduced (Figure 11e). The responses of 90th percentile wind speeds to PNA phase in the AOGCMs are likewise better (and more consistently) simulated for negative PNA conditions than for positive PNA conditions (cf. Figures 5b and 11f).

6. Summary and Discussion

In this study, we have investigated the response of wind speeds over the contiguous US to large-scale modes of climate variability including El Niño–Southern Oscillation (ENSO), the Arctic Oscillation (AO), and the Pacific–North American (PNA) pattern. For each mode, indices have been computed using reanalysis output and AOGCM simulations of the historical period (1950–2005) and used to define positive, neutral, and negative phases. Wind speeds at 500 hPa, 700 hPa, 850 hPa, and 10 m over the contiguous US have then been investigated according to the phase of each climate mode.

Consistent with prior research [e.g., Pryor and Ledolter, 2010], when computed from the NNR data, all three modes of climate variability exhibit strong teleconnections to mean midtropospheric wind speeds. Mean 500 hPa wind speeds are significantly different (at the 99% level) for both the positive minus neutral and the negative minus neutral phases of all three modes over large parts of the domain. The wind speed differences between each phase and neutral conditions are amplified when the 90th percentile values are considered. The response of 500 hPa wind speeds to ENSO phase is essentially symmetric with anomalies of opposite sign occurring during the warm and cold phases (Figure 3). The warm phase is associated with lower wind speeds over most of the US, while the cold phase is associated with higher wind speeds. Both phases of the AO and PNA are associated with higher 500 hPa wind speeds over most of the study. In accord with a priori expectations, near-surface (10 m) wind speeds exhibit more complex relationships with the climate modes. While in many cases, the 10 m wind speed anomalies are significant and of the same sign as their midtropospheric counterparts, in other cases (e.g., negative AO in the extreme southern US), the significant 10 m wind speed anomalies are of opposite sign to those at 500 hPa.

Spatial patterns and temporal indices for ENSO, AO, and PNA derived from daily output of 10 CMIP5 AOGCMs indicate that all models reproduced some aspects of these modes as derived from NNR—both in the spatial and temporal domains. The weakest agreement, in terms of both spatial pattern and temporal variability, is manifest in the ENSO index and teleconnection (Figures 6 and 10). Consistent with results from earlier CMIP experiments [e.g., Stoner *et al.*, 2009], the majority of models overestimate the variance explained by the AO. All AOGCMs exhibit a spatial pattern of AO similar to that from NNR (Figure 8), but 9 of the 10 AOGCMs exhibit patterns with too much spatial variability, either as a result of excessively low pressure in the polar center of action or excessively high pressure in the Pacific Ocean center of action (Figure 9b). The variance explained by the PNA pattern in the AOGCM output is in good agreement with the historical reanalysis data, but 9 of the 10 AOGCMs considered exhibit PNA patterns with too much spatial variability, usually related to the Pacific center of action but also occasionally resulting from the Atlantic center of action (Figures 7c and 9). This result differs from that of Stoner *et al.* [2009], who reported that most CMIP3 AOGCMs underestimated the magnitude of the PNA's Pacific center of action.

Despite the differences between the NNR and AOGCMs in terms of the detailed spatial and temporal characteristics of the climate modes considered, the models generally reproduce the response of wind speeds over the contiguous US to the phase of the climate modes as manifest in NNR. For the AO and PNA, the upper level (500 hPa) wind speeds exhibited a high degree of agreement with the response identified using historical reanalysis data. Specifically, for both the AO and PNA, at least 8 of the 10 AOGCMs exhibited responses of the same sign to both phases of the mode as the reanalysis data over nearly the entire contiguous US, although the AOGCM ensemble mean response was larger or smaller than the observed response for some regions. For ENSO, the 500 hPa wind speeds exhibited varied responses, sometimes in discord with relationships identified in the reanalysis data. Specifically, the response to El Niño is much better reproduced than the response to La Niña, despite a strong relationship in the NNR data. At 10 m, observed wind speed responses to the warm ENSO phase are limited to the southwestern region of the US and the high elevations of the Rocky Mountains. The former are reproduced in sign, but not in magnitude, by the AOGCMs, while the latter are not. The broad spatial response of the 10 m wind speeds to the cold ENSO phase is only reproduced by AOGCMs in parts of the southwest and in a narrow swath in the Great Plains. This result is consistent with the work of Sheffield *et al.* [2013b] who noted that the frequency of ENSO events in CMIP5 models was well produced but that teleconnections with near surface air temperature in North America were not.

Results presented herein are subject to the following important caveats. First, each of the large-scale modes of climate variability considered here exhibit variability at timescales that are not resolved by the 56 year record considered in this study (e.g., the decadal and multidecadal variability), and therefore, we are only

considering the component of the response related to shorter-term variability. Second, we use one reanalysis data set (NCEP-NCAR reanalysis) to derive the observed relationships. However, comparison with results from ECWMF ERA-Interim reanalysis over a common period (1979–2005) presented for the frequency domain work indicated a relatively high degree of accord with NNR (Figure 7) and yielded nearly identical results for the spatial patterns and time series of the indices presented in section 2 (not shown). Lastly, we have not considered the effects of interactions between these modes and ENSO. Forcing of PNA variability by ENSO has been the subject of several studies [see Yu, 2007]. Additional insights might also be gained by considering specific characteristics of ENSO, such as Modoki and Trans-Niño events [as in Lee *et al.*, 2013]. Sheffield *et al.* [2013b] noted that most CMIP5 AOGCMs are not able to produce the east and central Pacific types of ENSO events and their relationships with North American temperatures.

While acknowledging these important caveats, the primary conclusions of this analysis are as follows: (i) consistent with previous analyses based on near-surface observations or radiosonde data, there are strong teleconnections between the leading modes of large-scale climate variability and both near-surface and midtropospheric wind speeds over the contiguous US and (ii) the current generation AOGCMs are capable of reproducing at least some fraction of the wind climate variability that arises due to variations in the AO and PNA, but are less skillful in reproducing the influence of the ENSO, and particularly La Niña, on flow over the contiguous US. Our analyses shed light on the interactions between climate system processes operating at different spatial scales and may have important implications for development of regional wind projections using downscaled AOGCMs. By considering differences between the phases individually, rather than linear responses over the entire range of index values, we were able to identify asymmetric responses of wind speeds to positive and negative AO and PNA phases. Our results document the relationship between mean and 90th percentile wind speeds at multiple atmospheric levels and ENSO, AO, and PNA phases. Our findings add to the growing body of literature suggesting that information regarding changes in large-scale climate may be used to infer changes in regional wind speeds. These analyses have relevance for (i) those seeking to understand the dynamical links (teleconnections) between remote modes of climate variability and large-scale thermal and moisture advection and resulting changes in precipitation and streamflow over the contiguous US [e.g., Coleman and Budikova, 2013] and (ii) contextualizing sources of variability in projections of possible future climates.

Acknowledgments

This material is based upon work supported by the National Science Foundation under grants 1019603 and 1019620. Any opinions, findings, and conclusions or recommendations expressed in this material are those of the authors and do not necessarily reflect the views of the National Science Foundation. We acknowledge the World Climate Research Programme's Working Group on Coupled Modelling, which is responsible for CMIP, and we thank the climate modeling groups (listed in Table 1) for producing and making available their model output. For CMIP, the U.S. Department of Energy's Program for Climate Model Diagnosis and Intercomparison provides coordinating support and led development of software infrastructure in partnership with the Global Organization for Earth System Science Portals. The authors also gratefully acknowledge discussions with R.J. Barthelme and the thoughtful comments of three reviewers. In keeping with AGU's Data Policy, data used to produce the results of the paper are available from the author upon request.

References

- Ambaum, M. H. P., B. J. Hoskins, and D. B. Stephenson (2001), Arctic Oscillation or North Atlantic Oscillation?, *J. Clim.*, *14*, 3495–3506.
- Arora, V. K., J. F. Scinocca, G. J. Boer, J. R. Christian, K. L. Denman, G. M. Flato, V. V. Kharin, W. G. Lee, and W. F. Merryfield (2011), Carbon emission limits required to satisfy future representative concentration pathways of greenhouse gases, *Geophys. Res. Lett.*, *38*, L05805, doi:10.1029/2010GL046270.
- Ashok, K., T. P. Sabin, P. Swapna, and R. G. Murtugudde (2012), Is a global warming signature emerging in the tropical Pacific?, *Geophys. Res. Lett.*, *39*, L02710, doi:10.1029/2011GL050232.
- Bamzai, A. S. (2003), Relationship between snow cover variability and Arctic Oscillation index on a hierarchy of time scales, *Int. J. Climatol.*, *23*, 131–142.
- Bellouin, N., O. Boucher, J. Haywood, C. Johnson, A. Jones, J. Rae, and S. Woodward (2007), Improved representation of aerosols for HadGEM2. Hadley Centre technical note 73, Available from the online UK Met Office National Meteorological Library & Archive Online Catalogue.
- Burt, J. E., G. M. Barber, and D. L. Rigby (2009), *Elementary Statistics for Geographers*, Guilford Press, New York.
- Cohen, J., J. Foster, M. Barlow, K. Saito, and J. Jones (2010), Winter 2009–2010: A case study of an extreme Arctic Oscillation event, *Geophys. Res. Lett.*, *37*, L17707, doi:10.1029/2010GL044256.
- Coleman, J. S. M., and D. Budikova (2013), Eastern U.S. summer streamflow during extreme phases of the North Atlantic Oscillation, *J. Geophys. Res. Atmos.*, *118*, 4181–4193, doi:10.1002/jgrd.50326.
- Collins, W. J., et al. (2008), Evaluation of the HadGEM2 model, *Hadley Cent. Tech. Note 74*, Available from the online UK Met Office National Meteorological Library & Archive Online Catalogue.
- Cook, K. H., E. K. Vizi, Z. S. Launer, and C. M. Patricola (2008), Springtime intensification of the Great Plains low-level jet and Midwest precipitation in GCM simulations of the twenty-first century, *J. Clim.*, *21*, 6321–6340.
- Dee, D. P., et al. (2011), The ERA-Interim reanalysis: Configuration and performance of the data assimilation system, *Q. J. R. Meteorol. Soc.*, *137*, 553–597.
- Delworth, T. L., et al. (2006), GFDL's CM2 global coupled climate models. Part I: Formulation and simulation characteristics, *J. Clim.*, *19*, 643–674.
- Deser, C. (2000), On the teleconnectivity of the "Arctic oscillation", *Geophys. Res. Lett.*, *27*, 779–782, doi:10.1029/1999GL010945.
- Donner, L. J., et al. (2011), The dynamical core, physical parameterizations, and basic simulation characteristics of the atmospheric component AM3 of the GFDL Global Coupled Model CM3, *J. Clim.*, *24*, 3484–3519.
- Dufresne, J.-L., et al. (2012), Climate change projections using the IPSL-CM5 Earth System Model: From CMIP3 to CMIP5, *Clim. Dyn.*, *40*, 2123–2165, doi:10.1007/s00382-012-1636-1.
- Eichler, T., and W. Higgins (2006), Climatology and ENSO-related variability of North American extratropical cycle activity, *J. Clim.*, *19*, 2076–2093.
- Enloe, J., J. J. O'Brien, and S. R. Smith (2004), ENSO impacts on peak wind gusts in the United States, *J. Clim.*, *17*, 1728–1738.
- Feldstein, S. B. (2002), Fundamental mechanisms of PNA teleconnection pattern growth and decay, *Q. J. R. Meteorol. Soc.*, *128*, 775–796.

- Griffiths, M. L., and R. S. Bradley (2007), Variations of twentieth-century temperature and precipitation extreme indicators in the northeast United States, *J. Clim.*, *20*, 5401–5417, doi:10.1175/2007JCLI1594.1.
- Grise, K. M., S.-W. Son, and J. R. Gyakum (2013), Intraseasonal and interannual variability in North American storm tracks and its relationship to equatorial Pacific variability, *Mon. Weather Rev.*, *141*, 3610–3625.
- Iversen, T., et al. (2013), The Norwegian Earth System Model, NorESM1-M. Part 2: Climate response and scenario projections, *Geosci. Model Dev.*, *6*, 1–27.
- Ji, D., et al. (2014), Description and basic evaluation of BNU-ESM version 1, *Geosci. Model Dev. Discuss.*, *7*, 1601–1647.
- Kalnay, E., et al. (1996), The NCEP/NCAR 40-year reanalysis project, *Bull. Am. Meteorol. Soc.*, *77*, 437–470.
- Kim, S. T., and J.-Y. Yu (2012), The two types of ENSO in CMIP5 models, *Geophys. Res. Lett.*, *39*, L11704, doi:10.1029/2012GL052006.
- Klink, K. (2007), Atmospheric circulation effects on wind speed variability at turbine height, *J. Appl. Meteorol. Climatol.*, *46*, 445–456.
- L'Heureux, M., A. Butler, B. Jha, A. Kumar, and A. Wang (2010), Unusual extremes in the negative phase of the Arctic Oscillation during 2009, *Geophys. Res. Lett.*, *37*, L10704, doi:10.1029/2010GL043338.
- Langenbrunner, B., and J. D. Neelin (2013), Analyzing ENSO teleconnections in CMIP models as a measure of model fidelity in simulating precipitation, *J. Clim.*, *26*, 4431–4446.
- Leathers, D. J., B. Yarnal, and M. A. Palecki (1991), The Pacific/North American teleconnections pattern and United States climate. Part I: Regional temperature and precipitation associations, *J. Clim.*, *4*, 517–528.
- Lee, S.-K., R. Atlas, D. Enfield, C. Wang, and H. Liu (2013), Is there an optimal ENSO pattern that enhances large-scale atmospheric processes conducive to tornado outbreaks in the United States?, *J. Clim.*, *26*, 1626–1642.
- Lee, S.-K., B. E. Mapes, C. Wang, D. B. Enfield, and S. J. Weaver (2014), Springtime ENSO phase evolution and its relation to rainfall in the continental U. S., *Geophys. Res. Lett.*, *41*, 1673–1680, doi:10.1002/2013GL059137.
- Li, X., S. Zhong, X. Bian, and W. E. Heilman (2010), Climate and climate variability of the wind power resources in the Great Lakes region of the United States, *J. Geophys. Res.*, *115*, D18107, doi:10.1029/2009JD013415.
- Martin, G. M., et al. (2011), The HadGEM2 family of Met Office Unified Model climate configurations, *Geosci. Model Dev.*, *4*, 723–757.
- Pryor, S. C., and R. J. Barthelmie (2014), Hybrid downscaling of wind climates over the eastern USA, *Environ. Res. Lett.*, *9*, 024013.
- Pryor, S. C., and J. Ledolter (2010), Addendum to “Wind speed trends over the contiguous USA”, *J. Geophys. Res.*, *115*, D10103, doi:10.1029/2009JD013281.
- Pryor, S. C., R. J. Barthelmie, N. E. Clausen, M. Drews, N. MacKellar, and E. Kjellstrom (2012a), Analyses of possible changes in intense and extreme wind speeds over northern Europe under climate change scenarios, *Clim. Dyn.*, *38*, 189–208.
- Pryor, S. C., R. J. Barthelmie, and J. T. Schoof (2012b), Past and future wind climates over the contiguous USA based on the North American Regional Climate Change Assessment Program model suite, *J. Geophys. Res.*, *117*, D19119, doi: 10.1029/2012JD017449.
- Sheffield, J., et al. (2013a), North American climate in CMIP experiments. Part I: Evaluation of historical simulations of continental and regional climatology, *J. Clim.*, *26*, 9209–9245.
- Sheffield, J., et al. (2013b), North American climate in CMIP5 experiments. Part II: Evaluation of historical simulations of intraseasonal to decadal variability, *J. Clim.*, *26*, 9247–9290.
- Sheridan, S. C. (2003), North American weather-type frequency and teleconnections indices, *Int. J. Climatol.*, *23*, 27–45.
- St. George, S., and S. A. Wolfe (2009), El Niño stills winter winds across the southern Canadian Prairies, *Geophys. Res. Lett.*, *36*, L23806, doi:10.1029/2009GL041282.
- Stephenson, D. B., V. Pavan, M. Collins, M. M. Junge, R. Quadrelli, and participating CMIP2 modelling groups (2006), North Atlantic Oscillation response to transient greenhouse gas forcing and the impact on European winter climate: A CMIP2 multi-model assessment, *Clim. Dyn.*, *27*, 401–420.
- Stevens, B., et al. (2013), The atmospheric component of the MPI-M Earth System Model: ECHAM6, *J. Adv. Model. Earth Syst.*, *5*, 146–172, doi:10.1002/jame.20015.
- Stoner, A. M. K., K. Hayhoe, and D. J. Wuebbles (2009), Assessing general circulation model simulations of atmospheric teleconnections patterns, *J. Clim.*, *22*, 4348–4372.
- Taylor, K. E. (2001), Summarizing multiple aspects of model performance in a single diagram, *J. Geophys. Res.*, *106*, 7183–7192, doi:10.1029/2000JD900719.
- Taylor, K. E., R. J. Stouffer, and G. A. Meehl (2012), An overview of CMIP5 and the experimental design, *Bull. Am. Meteorol. Soc.*, *93*, 485–498.
- Trenberth, K. E. (1997), The definition of El Niño, *Bull. Am. Meteorol. Soc.*, *78*, 2771–2777.
- Voldoire, A., et al. (2012), The CNRM-CM5.1 global climate model: Description and basic evaluation, *Clim. Dyn.*, *40*, 2091–2121.
- von Salzen, K., et al. (2013), The Canadian Fourth Generation Atmospheric Global Climate Model (CanAM4). Part I: Representation of physical processes, *Atmosphere-Ocean*, *51*, 104–125.
- Wallace, J. M., and D. S. Gutzler (1981), Teleconnections in the geopotential height field during the Northern Hemisphere winter, *Mon. Weather Rev.*, *109*, 784–812.
- Wallace, J. M., and D. W. J. Thompson (2002), The Pacific center of action of the Northern Hemisphere annular mode: Real or artifact?, *J. Clim.*, *15*, 1987–1991.
- Weaver, S. J., and S. Nigam (2008), Variability of the Great Plains low level jet: Large-scale circulation context and hydroclimate impacts, *J. Clim.*, *21*, 1532–1550.
- Wolter, K., and M. S. Timlin (1993), Monitoring ENSO in COADS with a seasonally adjusted principal component index, paper presented at 17th Climate Diagnostics Workshop, NOAA/NMC/CAC, NSSL, Oklahoma Clim. Surv., CIMMS and the School of Meteor., Univ. of Oklahoma, Norman.
- Wu, T. (2012), A mass-flux cumulus parameterization scheme for large-scale models: Description and test with observations, *Clim. Dyn.*, *38*, 725–744.
- Xin, X., T. Wu, J. Li, Z. Wang, W. Li, and F. Wu (2012), How well does BCC_CSM1.1 reproduce the 20th century climate change over China?, *Atmos. Ocean. Sci. Lett.*, *6*, 21–26.
- Yu, B. (2007), The Pacific-North American pattern associated diabatic heating and its relationship to ENSO, *Atmos. Sci. Lett.*, *8*, 107–112.
- Yukimoto, S., et al. (2012), A new global climate model of the Meteorological Research Institute: MRI-CGCM3—Model description and basic performance, *J. Meteorol. Soc. Jpn.*, *90A*, 23–64.